Vortex-Induced Vibrations of Low Mass Ratio Cylindrical Cantilever Beams

Clara Vanessa Encke, Ersegun Deniz Gedikli
Department of Ocean and Resources Engineering, University of Hawai'i at Manoa
Honolulu, Hawai'i, USA

ABSTRACT

In this study, we conduct an experimental investigation into the dynamic response of two hollow cylindrical cantilever beams that are sealed with plastic caps at the end and are subjected to vortex-induced vibrations. We conducted experiments using two polycarbonate cylinders with mass ratios of 0.761 and 0.922 and damping ratios of 0.037 and 0.045, respectively. Motion analysis was performed using two high-speed cameras, and motion tracking was facilitated by UV lights for better image quality. Our findings indicate that the IL: CF frequency ratios conform to the conventional 2:1 frequency ratio. However, we also observed 1:1 and 3:1 frequency ratios at low and high reduced velocities. These were accompanied by predominantly small positive and negative lift coefficients in phase with velocity values. The amplitude response aligns with previous literature, although our study shows that the in-line amplitudes reach higher values due to the cylinders' low mass and damping ratios. We observed that at reduced velocities below 3, one of the cylinders showed higher in-line amplitudes than cross-flow.

KEY WORDS:

Vortex-induced Vibrations, Low-Mass Ratio, Low-Damping Ratio, Cantilever Cylinder

INTRODUCTION

Vortex-induced vibration (VIV) is a common issue seen in many marine structures, including offshore risers, offshore platform legs, cables, wind turbines, and others. When interacting with fluid, vortices form behind them. These vortices produce a low-pressure region, resulting in fluctuating hydrodynamic forces, hence VIV. When vibrations are not monitored or considered during the design process, they can cause fatigue, downtime in operations, and even catastrophic failures. Previously, VIV of rigid bodies has been studied extensively. Review papers such as Bearman (1984), Sarpkaya (2004), Williamson and Govardhan (2004) discuss the fundamental nature of VIV, and recent studies such as Bearman (2011), Liu et al. (2020), and Aktosun et al. (2024) discuss the effects of combined in-line and cross-flow motions on this complex dynamical system.

In VIV, the system depends mainly on two parameters: the mass ratio (m^*), which is defined as the cylinder's mass divided by the displaced fluid mass and the damping ratio (Khalak & Williamson, 1997; Pan et al., 2007). Khalak and Williamson (1997) explored low mass and damping ratio cylinders in the cross-flow direction, discovering the upper and lower VIV response branches. Later, Khalak and Williamson (1999) introduced a map of vortex modes with dimensionless amplitude, where the response amplitude is normalized by the cylinder diameter as a function of the normalized velocity. Govardhan and Williamson (2000) then studied the cross-flow VIV of an elastically mounted rigid cylinder in a fluid flow to gain more in-depth insights into these modes. Later, Flemming and Williamson (2005) looked at the in-line and the cross-flow directions where the cylinder was pivoted and added a third axis to the map of modes, concluding that the in-line direction is an important aspect of the overall emerging vortex modes. Moreover, because the cylinder was pivoted, they concluded that the observed response branches exist in different parameter spaces where the upper branch with the higher cross-flow motion corresponds to different vortex formation modes and forces, suggesting the fluid-structure interaction along the spanwise direction is very complex.

In this work, we use circular hollow cylinders with low mass and damping ratios and conduct experiments in a recirculating flow channel. Unlike Flemming and Williamson (2005), the cylinders are hollow (sealed with plastic caps at the end) and are directly fixed to the top of the tank with a clamp mechanism without using a thin, flexible pin. The system's oscillating mass and natural frequencies are equal in both in-line and cross-flow directions. Motion is captured using high-speed cameras under UV lights and then analyzed using motion tracking for post-processing.

MATERIALS AND METHODS

The experiments were conducted in a newly built recirculating water tank located in the Fluid-Structure Interactions and Nonlinear Dynamics (FSINLD) laboratory at the University of Hawai'i Manoa. The test cylinder is fixed from the top, keeping the other end free. Current is simulated by generating a uniform flow in the testing section, where the cylinder is partially submerged. In the experiments, the flow speed is first increased systematically, and the cylinder's motion is captured using high-speed cameras for further analysis.

The working principle of the small recirculating tank is simple. It houses a turbine connected to a motor, as shown in Figure 1. The turbine creates a flow by pushing the water that passes through it in one direction. In this direction, the water passes through a flow straightener before being directed through a shorter but finer flow straightener following a $180°$ curve in the tank. The measured flow speeds across the length and width using a flowmeter confirm the uniform flow conditions. The finer flow straightener is made of a $15cm$ long honeycomb structure of straws with

the purpose of creating a uniform flow and eliminating turbulences created by the turbine or the tank's curve. The test section starts after this flow straightener and is roughly $55cm$ long with a $20\ x\ 20\ cm$ cross-section. A second 180° curve leads the water back through the turbine. Figure 1a illustrates the experimental setup with the test cylinder, and Figure 1b shows the sketch of the whole tank along with the flow straightener and cylinder location. The test cylinders are painted black and marked with white dots along the length in both in-line and cross-flow directions for easy tracking, as illustrated in Figure 1a. The white markers were placed 2 cm apart, and each marker was comprised of around 15-20 pixels. High-speed cameras tracked the motion in both in-line and cross-flow directions with a frame rate of $240Hz$. High-speed cameras were placed orthogonal to each other for easy post-processing. After the videos are recorded for varying flow speeds, motion is analyzed using ProAnalyst motion tracking software.

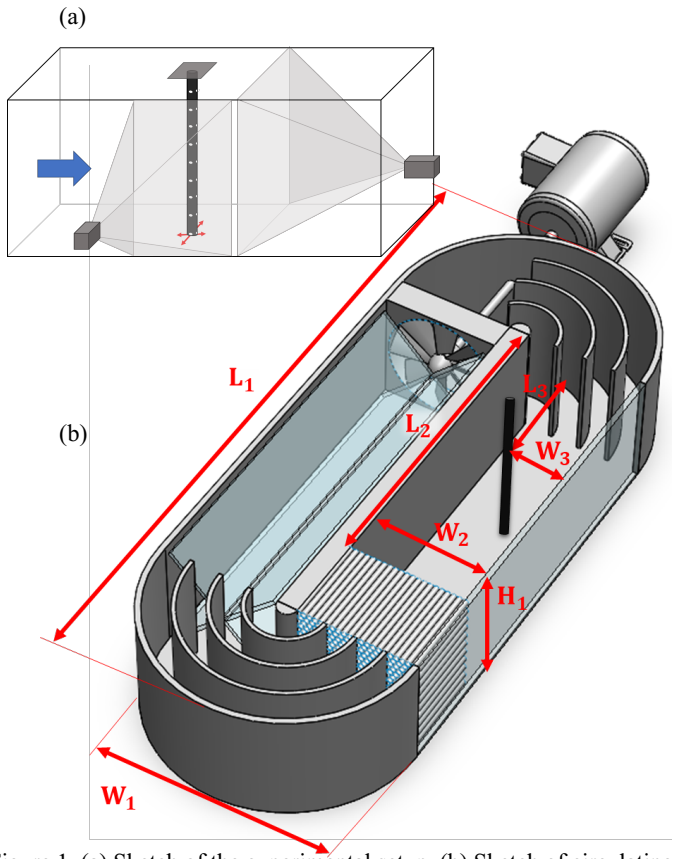

Figure 1. (a) Sketch of the experimental setup. (b) Sketch of circulating flow tank.

Experiments

Figure 2 shows the detailed experimental setup, in which the cylinders are placed downstream in the tank and attached to a clamp mechanism at the top. The bottom of each cylinder was kept close to the bottom of the tank (~ 2mm) to reduce the boundary effect. The top of the tank was closed with an acrylic lid to reduce the wave formations. The cylinder is fixed in position within the test section by a 3D-printed clamping system above the surface on an opening in the flow tank's lid. Since the cylinder is partly submerged, there are different characteristic heights such as H_1, which describes the overall water depth; H_2, which describes the height of the submerged part of the tested cylinder and therefore defines the effective length; H_3 represents the length of the cylinder's free end from the point of fixation to the end. H_4 describes the total length of the cylinder, and H_5 stands for the resulting height between the tank bottom and the cylinder. Table 1 shows all the relevant dimensions of the tank. The cylinders' natural frequencies were tested using pluck tests in air and water. Since the tested cylinders have symmetrical cross-sections, the natural frequency is the same in either direction. The damping ratios for two cylinders, Cylinder A and Cylinder B, are estimated to be 0.037 and 0.045, respectively.

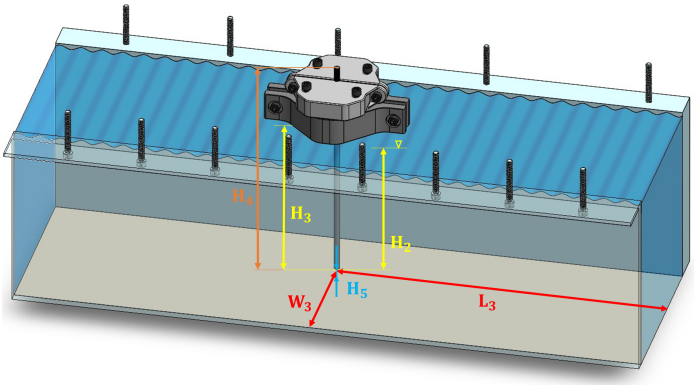

Figure 2. Experimental setup in the tank's test section with the clamp mechanism.

Table 1. Dimensions in the tank.

Abbreviation	Dimension (cm)
L_1	130.5
L_2	54.9
L_3	36
W_1	50.8
W_2	20
W_3	10
H_1	20
H_2	19.6
H_3	23.5
H_4	30.5
H_5	0.2

The flow speed in the experiments varied between 0.05 and 1 m/s. Due to a lack of movement at lower speeds and bubble formations at higher speeds, only motion at flow speeds up to $0.71m/s$ was analyzed. The test cylinders are made of extruded polycarbonate with a known elastic modulus of 2.38 GPa. Cylinder's mass ratio, m*, is defined by the ratio of the moving mass of the system (m_{system}), which is the weight of the cylinder from its fixed point to its free end over the mass of the fluid displaced by the partly submerged cylinder ($m_{displaced}$) (Khalak & Williamson, 1997). The test cylinders have an estimated mass ratio of 0.761 and 0.922, which is close to the critical mass ratio of 0.54. This is important because it is known that the synchronization between shedding and vibration frequencies hinges significantly on the fluctuation in hydrodynamic mass. Maintaining a low mass ratio typically leads to broader lock-in regions (Govardhan & Williamson, 2000; Sumer & Fredsoe, 2006; Vikestad, 1998).

To describe the flow around the body and calculate the hydrodynamic coefficients later on, the Reynolds number, $Re = UD/\upsilon$, is calculated for each flow speed, where υ represents the kinematic viscosity of the water.

This results in theoretical Reynolds numbers between 336 and 4767 for the 'Cylinder A' and between 224 and 3178 for the 'Cylinder B' which has a smaller outer diameter as shown in Table 2. Assuming a Strouhal number (St) of 0.22, the theoretical frequencies at which shedding occurs ($f_V = StU/D$) range from 1.83 Hz to 26.03 Hz for Cylinder A and from 2.75 Hz to 39.05 Hz for Cylinder B.

Table 2. Test dimensions and characteristics

		Cylinder A	Cylinder B
Outer-Diameter (mm)		6	4
Inner-Diameter (mm)		4	2
Material		Polycarbonate	Polycarbonate
Reynolds number (Re)		336 to 4767	224 to 3178
Total length (H_1)		308 mm	305.5 mm
Total weight		6.61 g	3.53 g
E-modulus		2.38 GPa	2.38 GPa
Aspect Ratio (H_2/D)		32.67	49
Mass Ratio (m^*)		0.761	0.922
Damping Ratio (ζ)		0.037	0.045
Theoretical f_V		1.83 to 26.03 Hz	2.75 to 39.05 Hz
Natural frequency	Air	25.8 Hz	16.08 Hz
	Water	17.38 Hz	10.94 Hz

Table 2 presents all relevant dimensions and characteristics of the tested cylinders. Here, the aspect ratio is defined by the ratio of the submerged cylinder length (effective cylinder length) over the cylinder's outer diameter.

Motion analysis

Motion tracking is carried out using the ProAnalyst software, which operates with a subpixel level of precision by tracing the center point of a pixel bulb within a search box (E. D. Gedikli, 2017). During the process of image analysis, a number of filter layers were applied to guarantee that the markers are visible and of a quality that allows them to be tracked. A threshold operation was the primary filter that was applied, and it was used to set all of the image pixels that were below the threshold to black (zero), while all of the image pixels that were above the threshold were set to white (255). As a result of the different lighting conditions in the room, the threshold value was slightly different in each instance.

In addition, a new motion-tracking setup was developed to enhance the visibility of the markers where UV black lights were utilized in conjunction with UV white paint to reactivate the ultraviolet light. The objective of this strategy was to diminish the visual disturbances that were brought by potential bubbles at high speeds while simultaneously enhancing the brightness of the tracking points. However, we decided to eliminate high-speed responses due to concerns that a large number of bubble formations could affect motion.

Another important challenge was that even though the two cameras were operated using the same remote, some of the resulting video data did not end up being perfectly synchronized during the experiments. As a result, the two signals still needed to be synchronized for motion analysis. The biggest challenge here was the oscillation frequency in both directions was not the same as the fundamental feature of the VIV and varied significantly as the flow speed varied. Hence, we developed a simple time-delay algorithm that delays one signal and correlates with the other. More specifically, to synchronize two signals depicting the same motion from different perspectives, we first identify common features in both signals, such as peaks or valleys. After calculating the time delay between these features to determine the synchronization offset, we apply a time delay to each signal, moving it forward or backward on the calculated offset (Li et al., 2020). Following that, we visually evaluate the synchronization and adjust the time delay as needed to achieve optimal signal alignment, allowing for precise analysis and comparison. Then, the motion in the in-line direction is plotted against the cross-flow motion to illustrate the resulting Lissajous shape, as illustrated in Figures 4 and 5.

RESULTS AND DISCUSSION

Figure 3 shows the amplitude and frequency response map obtained from experiments. The top image represents the normalized in-line amplitude response, the center image represents the normalized cross-flow amplitude response, and the bottom image represents the normalized frequency versus normalized reduced velocity.

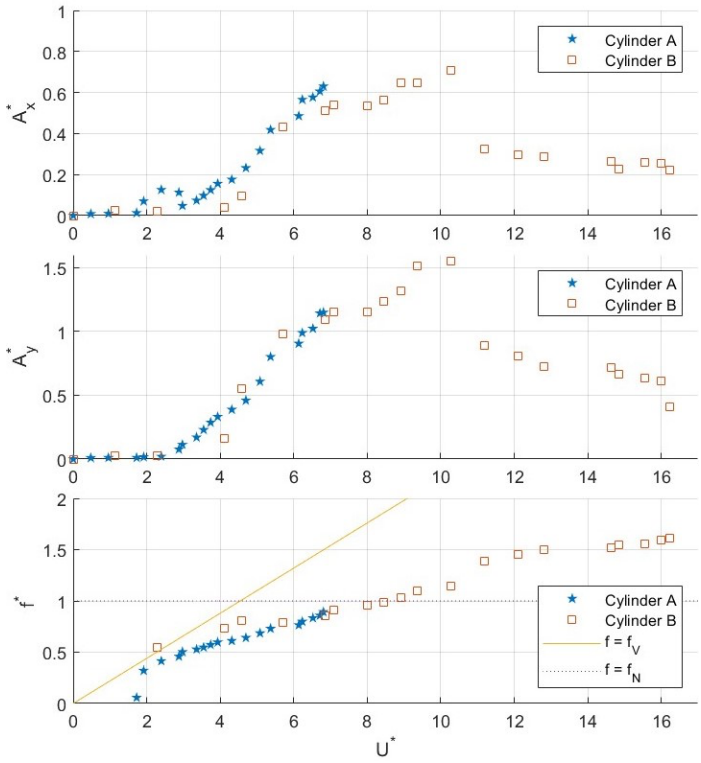

Figure 3. Top image: Non-dimensional in-line amplitude response (A_x^*) vs. normalized reduced velocity (U^*). Center image: Non-dimensional cross-flow amplitude response (A_y^*) vs. normalized reduced velocity (U^*). Bottom image: Normalized frequency ($f^* = f_y/f_N$) vs. normalized reduced velocity (U^*).

The normalized reduced velocity is established as the ratio of the flow speed to the product of the cylinder's diameter and its first mode natural frequency ($U^* = U/f_N D$). f_V is the vortex shedding frequency. Additionally, we use the concept of true reduced velocity for hydrodynamic force calculations, wherein the oscillation frequency replaces the natural frequency in the calculation. This reduced velocity ($V_r = U/fD$) allows for flexibility in defining the flow-induced motion concerning the oscillation frequency. Specifically, in the in-line

direction, the true reduced velocity is denoted as $V_{rx} = U/f_x D$, while in the cross-flow direction, it is represented as $V_{ry} = U/f_y D$. Sometimes this distinction is preferable since it facilitates a more comprehensive understanding of the structural response to varying flow conditions in different directions. Y-axes in the bottom image in Figure 3 represents the normalized oscillation frequency (f^*) where the oscillation frequency in the respective direction is normalized with the first mode natural frequency of the cylinder ($f^* = f_{x,y}\ /f_N$).

It's important to note that our analysis only extended to a flow speed of $0.71\ m/s$, leading to a limited response map for Cylinder A. To fully explore the VIV phenomenon, we conducted a second set of experiments using Cylinder B (see Table 2), which has a smaller mass and comparable mass damping ratio. This cylinder is specifically chosen to capture the complete VIV range across normalized reduced velocities. It's worth noting that the smaller mass cylinder also played a crucial role in having the peak amplitude observed in the system response in the in-line direction. Throughout our observations, we identified Initial (I), Upper (U), and Lower (L) branch regimes. Notably, while the response amplitudes and branches resembled those observed in Flemming and Williamson (2005), they resulted in a wider and higher amplitude response region. This variation can be attributed to disparities in mass and damping ratios, which resulted in wider VIV regions (Flemming & Williamson, 2005; Sumer & Fredsoe, 2006). This phenomenon is particularly pronounced when the mass ratio approaches the critical value of 0.54, as highlighted by Govardhan and Williamson (2004). Below this critical threshold, there is no decoherence region, and VIV manifests across all velocities beyond the initial lock-in point. Additionally, the frequency ratio followed the classic Strouhal frequency line (f_v) in the lower branch but deviated as the reduced velocity increased, as illustrated in the bottom image of Figure 3.

In Figure 3, the in-line amplitude response analysis shows that Cylinder A peaks around a normalized reduced velocity of 6.3. However, due to its slightly stiffer nature, the traditional amplitude-drop response isn't observed. Consequently, it's highly probable that the response would reach its maximum at slightly higher reduced velocities if we could conduct tests at even higher flow speeds. Conversely, Cylinder B demonstrates all three traditional response branches. The initial branch is observed at reduced velocities below 5.71, the upper branch coincides with reduced velocities between 5.71 and 10.28, and the lower branch appears at reduced velocities of 11.20 and higher. In the cross-flow direction, the cylinder reaches a normalized amplitude of 1.5, and in the in-line direction, it reaches a maximum amplitude of ~0.7, which is generally in line with observations of Flemming and Williamson (2005) although we reached much higher amplitude responses in the in-line direction. This is interesting because the total mass-damping ratio in their system is much lower than the current study, although the mass ratio in this work is much lower than the mass ratio they used. In addition, having a very low mass ratio resulted in a wider upper branch region, which resulted in a large response region between the normalized reduced velocities of 5.71 and 10.28. It is worth noting that at lower reduced velocities ($U^* \leq 4$), the in-line response may either surpass the cross-flow response or be comparable, as demonstrated by Cylinder A, although this phenomenon wasn't observed for Cylinder B. So, the onset conditions of this is unknown and still a research question which will be further investigated in the future. Yet, this finding is intriguing and aligns with similar results reported for bending-dominated cylinders (E. D. Gedikli, 2017; E. Gedikli et al., 2018).

Figures 4 and 5 illustrate the selected phase space patterns (Lissajous pattern) for 0.25 seconds of data for clarity. This demonstrates that as the flow speed increased, the cylinder's response amplitude increased, and the in-line contribution to the overall response became significant. More specifically, Cylinder A starts oscillating with a figure-eight pattern at around a reduced velocity of 3 and continues to oscillate with the same pattern as the flow speed increases, reaching a cross-flow amplitude of 1.2 and an inline amplitude of 0.6. In the meantime, Cylinder B exhibits a figure-eight motion pattern in the upper-branch region, which is distinguished by persistent oscillation and relatively high cross-flow amplitudes. The observed behavior continues until the reduced velocity value of 11, beyond which a clear phase portrait is no longer observable, as depicted in Figure 5.

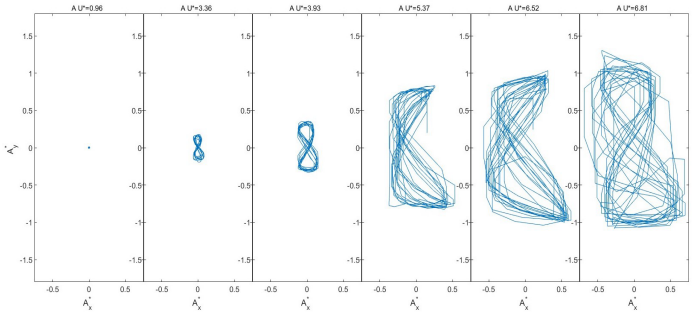

Figure 4. Lissajous shapes for Cylinder A for selected normalized reduced velocities. Motion represents the point at the far free end. Flow is from left to right.

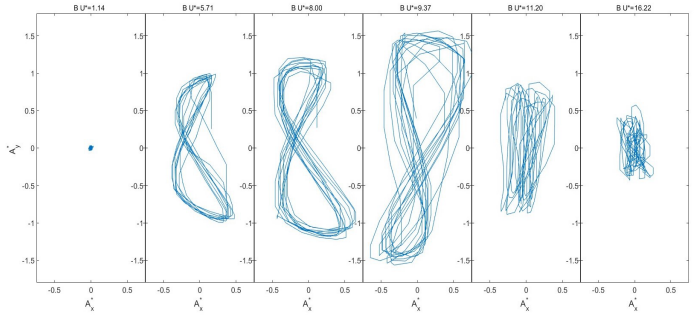

Figure 5. Lissajous shapes for Cylinder B for selected normalized reduced velocities. Motion represents the point at the far free end. Flow is from left to right.

Figures 6 and 7 show example motion time histories in in-line and cross-flow directions (top image) alongside frequency responses in the in-line (bottom left image) and cross-flow (bottom right image) directions. Figure 6 shows the response at normalized reduced velocity of 6.71 for Cylinder A where in-line frequency is twice the cross-flow frequency. Similarly, Figure 7 shows the Cylinder B's dynamic response at normalized reduced velocity of 6.86 where again in-line frequency is twice the cross-flow oscillation frequency. As a result, harmonic oscillations are evident in both directions despite the presence of a 1:1 in-line frequency component, which is not particularly significant.

Table 3 presents the frequencies of the cylinder's oscillation in both the cross-flow and in-line directions, along with the corresponding in-line to cross-flow frequency ratios (f_{IL}/f_{CF}). It is important to highlight that the cylinder's motion predominantly oscillated in the in-line direction and was greater than that observed in the cross-flow direction at flow speeds below $0.3\ m/s$ for Cylinder A. Consequently, the response in the in-line direction exhibited a more periodic behavior. In contrast, the motion in the cross-flow direction was quasi-periodic at lower speeds. As a result, both Cylinder A and Cylinder B generally exhibited dominant 2:1 in-line to cross-flow frequency ratios throughout the study. At the lowest reduced velocity of 1.92 for Cylinder A, the cylinder oscillated with 3:1

in-line to cross-flow frequency, and that ratio decreased as the reduced velocity increased, eventually settling at a 2:1 in-line to cross-flow frequency ratio after the reduced velocity of three. Gedikli et al. (2018) observed similar responses in low reduced velocities of bending-dominated flexible cylinder experiments undergoing VIV. Another important observation is that, between normalized reduced velocities of 11.20 and 16.22, the in-line frequency of the Cylinder B was close to three times that of the cross-flow frequency, rather than the expected doubling. Interestingly, this coincided with the onset of the lower branch region and persisted throughout the lower branch for all subsequent normalized reduced velocities. At low normalized reduced velocities, the N/A values signify motion characterized by an absence of steady response or non-harmonic motion, where no apparent dominant frequency is discernible.

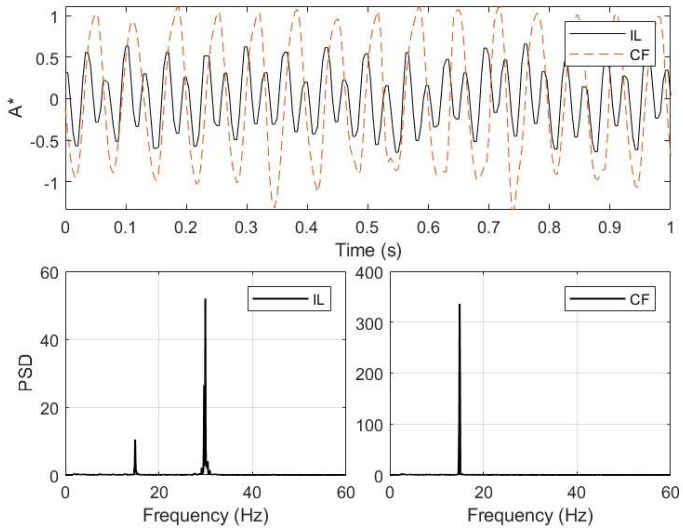

Figure 6. Top: Motion time history of Cylinder A in in-line (black line), and cross-flow (red-dashed line) directions at $U^* = 6.71$. Bottom Left: In-line frequency component. Bottom Right: Cross-flow frequency component.

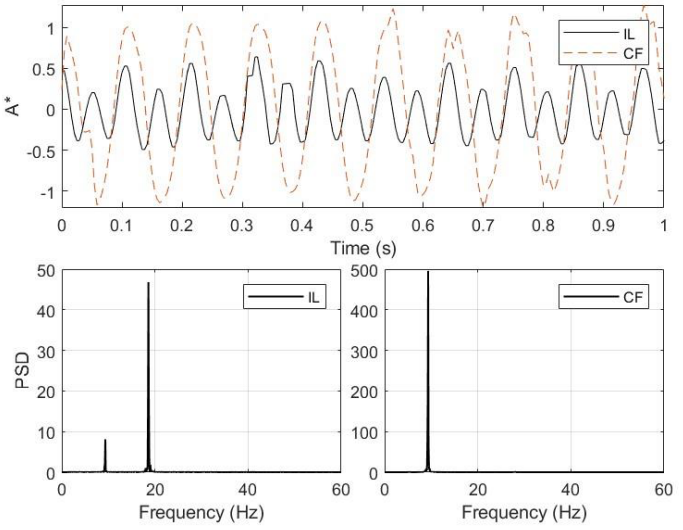

Figure 7. Top: Motion time history of Cylinder B in in-line (black line), and cross-flow (red-dashed line) directions at $U^* = 6.86$. Bottom Left: In-line frequency component. Bottom Right: Cross-flow frequency component.

Table 3. Oscillation frequencies in in-line and cross-flow directions for Cylinder A and Cylinder B at varying normalized reduced velocities.

Cylinder A				**Cylinder B**			
$\boldsymbol{U^*}$	f_{IL}	f_{CF}	f_{IL}/f_{CF}	U^*	f_{IL}	f_{CF}	f_{IL}/f_{CF}
$(-)$	(Hz)	(Hz)	$(-)$	$(-)$	(Hz)	(Hz)	$(-)$
0.48	N/A	N/A	N/A	**1.14**	N/A	N/A	N/A
0.96	N/A	N/A	N/A	**2.29**	N/A	6	N/A
1.73	N/A	N/A	N/A	**4.11**	N/A	8.06	N/A
1.92	16.71	5.57	3.00	**4.57**	17.66	8.83	2.00
2.40	17.40	7.46	2.33	**5.71**	17.40	8.66	2.01
2.88	18.26	7.97	2.29	**6.86**	18.60	9.34	1.99
2.97	18.26	8.74	2.09	**7.08**	19.89	9.94	2.00
3.36	18.26	9.17	1.99	**8.00**	20.91	10.46	2.00
3.55	19.03	9.51	2.00	**8.46**	21.60	10.80	2.00
3.74	19.89	9.94	2.00	**8.91**	22.80	11.31	2.02
3.93	20.66	10.37	1.99	**9.37**	24.00	12.00	2.00
4.32	21.34	10.63	2.01	**10.28**	25.20	12.51	2.01
4.70	22.29	11.14	2.00	**11.20**	50.06	15.17	3.30
5.08	23.74	11.91	1.99	**12.11**	49.46	15.86	3.12
5.37	25.29	12.69	1.99	**12.80**	49.37	16.46	3.00
6.14	26.57	13.29	2.00	**14.63**	49.03	16.63	2.95
6.23	27.77	13.89	2.00	**14.85**	48.77	16.89	2.89
6.52	29.06	14.49	2.01	**15.54**	48.60	17.06	2.85
6.71	29.91	14.91	2.01	**16.00**	48.43	17.40	2.78
6.81	31.03	15.51	2.00	**16.22**	48.26	17.66	2.73

Fluid Force Estimates and Motion Hydrodynamics

In order to gain a deeper insight into the hydrodynamic characteristics of the test cylinder, we employ a method wherein we estimate the total lift and drag forces. This estimation is based on applying the equation of motion typically used for a cantilever beam under sinusoidal loading conditions, while assuming minimal body motions, as in Gedikli and Dahl (2017) and Seyed-Aghazadeh and Modarres-Sadeghi (2016). This approach provides a practical means to estimate hydrodynamic forces when direct measurement isn't viable. However, its effectiveness greatly depends on accurately modeling the structural characteristics of the cylinder and making reasonable assumptions about its motion.

$$F_D(z,t) = m\frac{\partial^2 x}{\partial t^2} + \frac{\partial^2}{\partial z^2}\left(EI\frac{\partial^2 x}{\partial z^2}\right) \quad (1)$$

$$F_L(z,t) = m\frac{\partial^2 y}{\partial t^2} + \frac{\partial^2}{\partial z^2}\left(EI\frac{\partial^2 y}{\partial z^2}\right) \quad (2)$$

where F_D represents the estimated drag force, F_L represents the lift force. The variables x and y denote the in-line and cross-flow displacements with respect to time, respectively. Additionally, m represents the mass per length of the cylinder, E stands for the modulus of elasticity, I

represents the area moment of inertia, t denotes time, and z represents the spanwise spatial dimension.

Then, we use the estimated forces to derive lift and drag coefficients. Lift coefficient (C_L) and drag coefficient (C_D) is described as,

$$C_L = \frac{F_L(t)}{1/2\,\rho U^2 DL} \tag{3}$$

$$C_D = \frac{F_D(t)}{1/2\,\rho U^2 DL} \tag{4}$$

where ρ represents the flow density, U represents the flow speed, D represents the diameter of the cylinder, and L represents the cylinder's effective length (H_2). Once the lift and drag coefficients are estimated, we use them to estimate hydrodynamic force coefficients. To calculate the hydrodynamic force coefficients acting on a cylinder subjected to specific motions, we assume that the hydrodynamic lift force experienced by the moving cylinder is essentially a phase-shifted sinusoidal function. This approach allows us to separate the force into two distinct components. First, there is the non-dimensional force, denoted as CL_v, which is proportional to the cylinder's velocity and has the greatest influence on the structure's excitation. Second, there is a force associated with the cylinder's acceleration, known as CL_a, which essentially determines the system's effective mass (Sarpkaya, 1979). These components are calculated by taking the inner product of the lift coefficient and the velocity and acceleration of the cylinder, as described more in detail in Smogeli (2009) and Gedikli and Dahl (2014).

$$C_{L_v} = \sqrt{\frac{2}{T}}\frac{\langle C_L(t), \dot{y}(t)\rangle}{\sqrt{\langle \dot{y}(t), \dot{y}(t)\rangle}} \tag{5}$$

$$C_{L_a} = \sqrt{\frac{2}{T}}\frac{\langle C_L(t), \ddot{y}(t)\rangle}{\sqrt{\langle \ddot{y}(t), \ddot{y}(t)\rangle}} \tag{6}$$

where T is the window length for the inner product, C_L is the estimated lift force, and $\dot{y}$ and $\ddot{y}$ represent the velocity and acceleration values, respectively. One can also derive the added mass coefficient in the cross-flow direction, Cm_y, using the lift coefficient in phase with acceleration, and added mass in the in-line direction, C_{mx}, using the drag coefficient in phase with acceleration as:

$$C_{m_y} = \frac{-C_{L_a}\,V_{r_y}^2}{2\pi^3\,A_y^*} \tag{7}$$

$$C_{m_x} = \frac{-C_{D_a}\,V_{r_x}^2}{2\pi^3\,A_x^*} \tag{8}$$

It is important to keep in mind that these added mass coefficients represent the added mass at a specific reduced velocity and amplitude. This means that it is possible to determine the varying added mass along the length of the cylinder by varying these non-dimensional parameters that define the Cm_y and Cm_x.

Figures 8 and 9 present the specific hydrodynamic force coefficients for the cylinder's far-free endpoint in both in-line and cross-flow directions. The top figures in Figure 8 and Figure 9 represent C_{La} and C_{Da} values, and the bottom figure represents C_{Lv} and C_{Dv} values as a function of normalized reduced velocity for Cylinder A (blue triangles) and Cylinder B (red circles). Among these hydrodynamic coefficients, the lift coefficient in phase with the velocity, C_{L_v} indicates whether energy is being transferred from the fluid to the structure or vice versa. If C_{L_v} is positive, the system is generally receiving energy from the moving fluid, effectively causing it to vibrate, whereas if it is negative, the fluid is damping the system (Gopalkrishnan, 1993). Similarly, C_{Dv} illustrates in-line motions from free vibration when the coefficient is positive, while a negative coefficient indicates net energy transfer from the body to the fluid, indicating a forced vibration system. If these values are close to zero, energy is balanced between the fluid and the cylinder, hence free vibration. C_{La} and C_{Da} describe the effective added mass forces in the system (including potential flow added mass and effects of vortex formation in the wake of the cylinder).

Figures 8 and 9 indicate that the C_{Lv} and C_{Dv} values for both Cylinder A and Cylinder B remain close to zero throughout all the reduced velocities, suggesting free vibrations. However, there are some minor fluctuations between negative and positive values. C_{La} and C_{Da} values take on all positive values across all the reduced velocities. Moreover, for reduced velocity less than 3, C_{La} and C_{Da} values decrease towards higher reduced velocities and then start to increase towards the Upper branch region. For Cylinder B, C_{La} and C_{Da} values first increase in the Initial branch region, then fluctuate at higher values throughout the Upper branch region (between the normalized reduced velocities of 5.71 and 10.28), and then drop significantly in the Lower branch region.

Because C_{La} and C_{Da} values are positive for both cylinders, corresponding added mass values in both in-line and cross-flow directions are all negative. Moreover, added mass values in the cross-flow direction for "Cylinder A" increase in negative amplitudes after the reduced velocity of 2.97 as the normalized reduced velocity increases, reducing the effective mass of the system. For Cylinder B, added mass values in cross-flow directions are comparable to Cylinder A in the Initial and Upper Branch regions. In the Upper Branch region, added mass in the in-line direction increases, moving towards a positive direction, although it never takes a positive value.

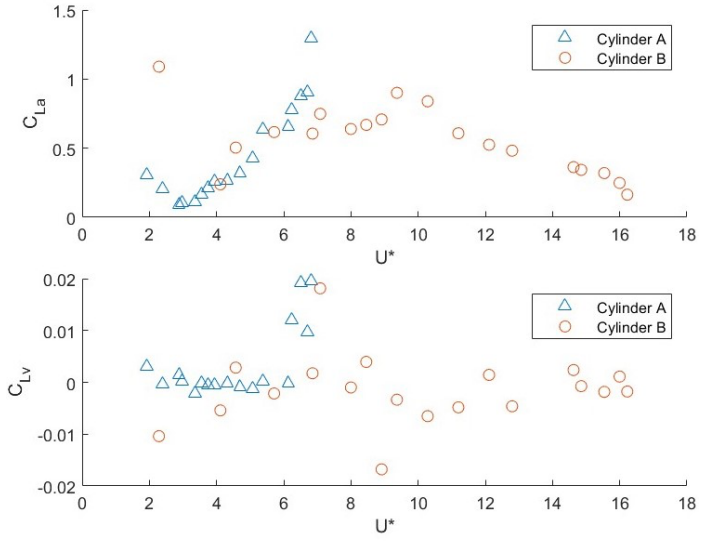

Figure 8. C_{La} and C_{Lv} over normalized reduced velocity U*.

As a result, at higher reduced velocities in the Upper Branch region, the impact of added mass appears to be more pronounced, with larger negative values observed in the cross-flow direction compared to the in-line direction. This suggests that negative added mass could potentially alter the frequency characteristics of the oscillations by shifting the natural frequency of the cylinder, potentially leading to larger

oscillations. It should be noted that we derived the total force using Euler-Bernoulli beam equations and assumed a force-motion balance. The motion response data used to estimate the forces encompass potential added mass and fluid effects. Therefore, while the results may lack precision, they offer a general understanding of the overall response.

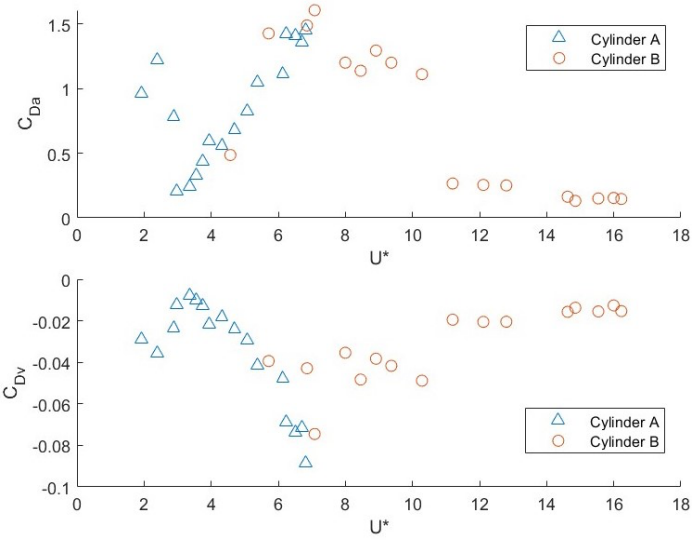

Figure 9. C_{Da} and C_{Dv} over normalized reduced velocity U*.

Table 4. Added mass coefficients for cross-flow and in-line directions at varying reduced velocities for Cylinder A and Cylinder B.

Cylinder A			**Cylinder B**		
U^*	C_{m_y}	C_{m_x}	U^*	C_{m_y}	C_{m_x}
0.48	N/A	N/A	**1.14**	N/A	N/A
0.96	N/A	N/A	**2.29**	-11.55	N/A
1.73	N/A	N/A	**4.11**	-0.73	N/A
1.92	-11.21	-0.88	**4.57**	-0.47	-0.65
2.40	-5.74	-0.90	**5.71**	-0.53	-0.69
2.88	-0.76	-0.84	**6.86**	-0.57	-0.76
2.97	-0.53	-0.56	**7.08**	-0.64	-0.73
3.36	-0.42	-0.54	**8.00**	-0.63	-0.63
3.55	-0.49	-0.57	**8.46**	-0.64	-0.60
3.74	-0.52	-0.60	**8.91**	-0.64	-0.59
3.93	-0.55	-0.67	**9.37**	-0.70	-0.55
4.32	-0.56	-0.63	**10.28**	-0.71	-0.50
4.70	-0.60	-0.64	**11.20**	-0.72	-0.08
5.08	-0.62	-0.58	**12.11**	-0.73	-0.10
5.37	-0.70	-0.55	**12.80**	-0.78	-0.11
6.14	-0.75	-0.60	**14.63**	-0.76	-0.11
6.23	-0.77	-0.62	**14.85**	-0.77	-0.10
6.52	-0.84	-0.60	**15.54**	-0.80	-0.11
6.71	-0.79	-0.55	**16.00**	-0.66	-0.11
6.81	-1.05	-0.54	**16.22**	-0.65	-0.14

CONCLUSION

In this work, two polycarbonate cylinders with low mass and damping ratios were subjected to VIV experiments in a recirculating water tank. Motion analysis was performed using high-speed cameras, and the results were analyzed to understand the cylinders' dynamic response to varying flow conditions.

The findings of this work are consistent with previous research, highlighting the importance of parameters such as mass and damping ratios in VIV analysis. Notably, the study showed intriguing deviations from conventional frequency ratios, highlighting the complexities of VIV phenomena. The experimental setup includes a fixed hollow cylinder to the tank, which improves motion analysis over previous methods. The use of UV lights and high-speed cameras also enhances visibility and precision.

Significant findings from our study include the observation of conventional IL: CF frequency ratios alongside deviations such as 1:1 and 3:1 frequency ratios at specific reduced velocities in different response branches. Moreover, the amplitude response, particularly in the in-line direction, reached higher values due to the cylinders' low mass and damping ratios. The smaller mass cylinder showcased a wider and higher amplitude response region, indicating a broader lock-in region. In addition, Cylinder A exhibited larger in-line oscillations than the cross-flow directions at reduced velocities lower than 3.

The analysis of hydrodynamic coefficients provided further information about fluid-structure interactions. Lift and drag force estimation, along with lift and drag coefficients, provide a better understanding of the cylinder's behavior under different flow conditions. For example, the added mass coefficients increase in the negative direction in the Upper Branch region and drop suddenly in the Lower Branch region at higher reduced velocities. This suggests that the effective added mass drops at large amplitudes, which may result in even larger responses. Another motivation for this work was to see if we could have a broader lock-in region, especially for structural optimization and potential energy harvesting applications. This is crucial, as broader lock-in regions offer the potential for harnessing more energy from the flow-induced vibrations, thus enhancing the efficiency of energy harvesting systems.

Future research endeavors should focus on expanding the scope of experiments to include a broader range of cylinder configurations and mass ratios. Additionally, investigating the onset conditions of in-line response surpassing cross-flow response at lower reduced velocities presents an intriguing avenue for further exploration. By deepening our understanding of VIV phenomena and its implications for structural optimization and energy harvesting, we can pave the way for more efficient and resilient marine structures and renewable energy systems. Another important point is that, future experiments with strain gauges and force sensors will yield more reliable data on the forces acting on the cylinder.

REFERENCES

Aktosun, E., Gedikli, E. D., & Dahl, J. M. (2024). Observed wake branches from the 2-DOF forced motion of a circular cylinder in a free stream. *Journal of Fluids and Structures*, *124*, 104035. https://doi.org/10.1016/j.jfluidstructs.2023.104035

Bearman, P. W. (1984). Vortex Shedding from Oscillating Bluff Bodies. *Annual Review of Fluid Mechanics*, *16*(1), 195–222. https://doi.org/10.1146/annurev.fl.16.010184.001211

Bearman, P. W. (2011). Circular cylinder wakes and vortex-induced vibrations. *Journal of Fluids and Structures*, *27*(5), 648–658. https://doi.org/10.1016/j.jfluidstructs.2011.03.021
Flemming, F., & Williamson, C. H. K. (2005). Vortex-induced vibrations of a pivoted cylinder. *Journal of Fluid Mechanics*, *522*, 215–252. https://doi.org/10.1017/S0022112004001831
Gedikli, E., Chelidze, D., & Dahl, J. (2018). Bending dominated flexible cylinder experiments reveal insights into modal interactions for flexible body vortex-induced vibrations. *Proceedings of the International Offshore and Polar Engineering Conference*, *2018-June*, 1003–1010.
Gedikli, E. D. (2017). *Dynamic Response and Active Control of Flexible Cylindrical Structures Undergoing Vortex-Induced Vibrations* [PhD Thesis, University of Rhode Island]. https://digitalcommons.uri.edu/oa_diss/631
Gedikli, E. D., Chelidze, D., & Dahl, J. M. (2018). Observed mode shape effects on the vortex-induced vibration of bending dominated flexible cylinders simply supported at both ends. *Journal of Fluids and Structures*, *81*, 399–417. https://doi.org/10.1016/j.jfluidstructs.2018.05.010
Gedikli, E. D., & Dahl, J. M. (2017). Mode excitation hysteresis of a flexible cylinder undergoing vortex-induced vibrations. *Journal of Fluids and Structures*, *69*, 308–322. https://doi.org/10.1016/j.jfluidstructs.2017.01.006
Gedikli, E., & Dahl, J. (2014). Mode shape variation for a low-mode number flexible cylinder subject to vortex-induced vibrations. *Proceedings of the International Conference on Offshore Mechanics and Arctic Engineering - OMAE*, *2*. https://doi.org/10.1115/OMAE2014-24232
Gopalkrishnan, R. (1993). *Vortex-induced forces on oscillating bluff cylinders* [Thesis, Massachusetts Institute of Technology]. https://dspace.mit.edu/handle/1721.1/12539
Govardhan, R., & Williamson, C. H. K. (2000). Modes of vortex formation and frequency response of a freely vibrating cylinder. *Journal of Fluid Mechanics*, *420*, 85–130. https://doi.org/10.1017/S0022112000001233
Khalak, A., & Williamson, C. H. K. (1997). Investigation of relative effects of mass and damping in vortex-induced vibration of a circular cylinder. *Journal of Wind Engineering and Industrial Aerodynamics*, *69–71*, 341–350. https://doi.org/10.1016/S0167-6105(97)00167-0
Khalak, A., & Williamson, C. H. K. (1999). Motions, forces and mode transitions in vortex-induced vibrations at low-mass damping. *Journal of Fluids and Structures*, *13*(7), 813–851. https://doi.org/10.1006/jfls.1999.0236
Li, H., Gedikli, E. D., & Lubbad, R. (2020). Exploring time-delay-based numerical differentiation using principal component analysis. *Physica A: Statistical Mechanics and Its Applications*, *556*, 124839. https://doi.org/10.1016/j.physa.2020.124839
Liu, G., Li, H., Qiu, Z., Leng, D., Li, Z., & Li, W. (2020). A mini review of recent progress on vortex-induced vibrations of marine risers. *Ocean Engineering*, *195*, 106704. https://doi.org/10.1016/j.oceaneng.2019.106704
Pan, Z. Y., Cui, W. C., & Miao, Q. M. (2007). Numerical simulation of vortex-induced vibration of a circular cylinder at low mass-damping using RANS code. *Journal of Fluids and Structures*, *23*(1), 23–37. https://doi.org/10.1016/j.jfluidstructs.2006.07.007
Sarpkaya, T. (1979). Vortex-Induced Oscillations: A Selective Review. *Journal of Applied Mechanics*, *46*(2), 241–258. https://doi.org/10.1115/1.3424537
Sarpkaya, T. (2004). A critical review of the intrinsic nature of vortex-induced vibrations. *Journal of Fluids and Structures*, *19*(4), 389–447. https://doi.org/10.1016/j.jfluidstructs.2004.02.005
Seyed-Aghazadeh, B., & Modarres-Sadeghi, Y. (2016). Reconstructing the vortex-induced-vibration response of flexible cylinders using limited localized measurement points. *Journal of Fluids and Structures*, *65*, 433–446. https://doi.org/10.1016/j.jfluidstructs.2016.06.006
Smogeli, O. N., Hover, F. S., & Triantafyllou, M. S. (2009). *Force-Feedback Control in VIV Experiments*. 685–695. https://doi.org/10.1115/OMAE2003-37340
Sumer, B. M., & Fredsoe, J. (2006). *Hydrodynamics Around Cylindrical Strucures*. World Scientific.
Vikestad, K. (1998). *Multi-frequency response of a cylinder subjected to vortex shedding and support motions* [PhD Thesis, Norwegian University of Science and Technology]. https://www.osti.gov/etdeweb/biblio/353150
Williamson, C. H. K., & Govardhan, R. (2004). Vortex-Induced Vibrations. *Annual Review of Fluid Mechanics*, *36*(1), 413–455. https://doi.org/10.1146/annurev.fluid.36.050802.122128